THE JOURNAL OF BIOLOGICAL CHEMISTRY VOL. 284, NO. 52, pp. 36557–36568, December 25, 2009
© 2009 by The American Society for Biochemistry and Molecular Biology, Inc. Printed in the U.S.A.

Integrin Activation Dynamics between the RGD-binding Site and the Headpiece Hinge*

Received for publication, July 4, 2009, and in revised form, September 8, 2009 Published, JBC Papers in Press, September 17, 2009, DOI 10.1074/jbc.M109.041194

Eileen Puklin-Faucher[1] **and Viola Vogel**[2]
From the Department of Materials, Laboratory of Biologically Oriented Materials, ETH, Zurich CH-8049, Switzerland

Integrins form mechanical links between the extracellular matrix and the cytoskeleton. Although integrin activation is known to be regulated by an allosteric conformational change, which can be induced from the extracellular or intracellular end of the molecule, little is known regarding the sequence of structural events by which signals propagate between distant sites. Here, we reveal with molecular dynamics simulations of the FnIII$_{10}$-bound $\alpha_V\beta_3$ integrin headpiece how the binding pocket and interdomain βA/hybrid domain hinge on the distal end of the βA domain are allosterically linked via a hydrophobic T-junction between the middle of the α1 helix and top of the α7 helix. The key results of this study are: 1) that this T-junction is induced by ligand binding and hinge opening, and thus displays bidirectionality; 2) that formation of this junction can be accelerated by ligand-mediated force; and 3) how formation of this junction is inhibited by Ca^{2+} in place of Mg^{2+} at the site adjacent to the metal ion-dependent adhesion site ("ADMIDAS"). Together with recent experimental evidence that integrin complexes can form catch bonds (*i.e.* become strengthened under force), as well as earlier evidence that Ca^{2+} at the ADMIDAS results in lower binding affinity, these simulations provide a common structural model for the dynamic process by which integrins become activated.

Integrins anchor cells to the extracellular matrix. They are transmembrane heterodimers, composed of non-covalently bound α and β subunits that associate to form the extracellular, ligand-binding head, two multidomain "legs," two single-pass transmembrane helices, and two short cytoplasmic tails (Fig. 1*A*). All known integrin heterodimers contain the βA domain (also called I-like or βI domain), located at the extracellular end of the β-subunit. The top of the βA domain contains three metal ion binding sites, termed the "ligand-induced metal binding site" ("LIMBS"),[3] the "metal ion-dependent adhesion site" ("MIDAS"), and the "adjacent to the MIDAS" ("ADMIDAS"). The LIMBS has been called the synergistic metal binding site instead, since it was found to contain a metal ion in a crystal structure of the unliganded $\alpha_{IIb}\beta_3$ integrin (44).

Integrin-mediated adhesion often occurs under tensile forces such as fluid flow or myosin-mediated contractions that cells exert to sample the rigidity of their surroundings. Thus, to enable mechanosensing, integrins cannot be constitutively active. Rather, integrin activation is regulated by long-range conformational changes that can originate from the cytoplasmic or extracellular end of the integrin molecule (1). For example, ligand binding has been shown to induce the activating conformational change that leads to hinge opening between the βA and hybrid domains in the integrin headpiece (2–4). Vice versa, events originating from the cytoplasmic region of the molecule have been shown to switch the extracellular binding site to the high affinity state (5). This bidirectional reciprocity is typical for allosterically regulated proteins (6).

Although many factors that regulate the allosteric pathway of integrin activation are known, such as ligand binding (7), divalent cations (8), and mechanical force (9, 10), *how* structural alterations propagate from one end of the molecule to the other remains poorly understood. For instance, x-ray crystallographic structures of the unliganded $\alpha_v\beta_3$ (11) and liganded $\alpha_{IIb}\beta_3$ (12) integrins provide snapshots of the closed and open headpiece hinge conformations, respectively. These differences highlight the structural events that accompany activation. Yet little is known regarding the sequence by which these events occur. In another example, comparison between the liganded $\alpha_v\beta_3$ (11) and liganded $\alpha_{IIb}\beta_3$ (12) integrin crystal structures reveals near identical configurations of the ligand-bound β_3 integrin binding pocket, differing only in the backbone hydrogen bonding of the β1-α1 loop (see Fig. 1*E*) (12, 13). However, these structures display a ~62° difference in the hinge angle between the βA and hybrid domains, a conformational change that has been shown to govern binding affinity (2–4).

With no experimental techniques currently available to obtain dynamic, atomic level insights into the integrin activation pathway, we used molecular dynamics (MD) simulations and steered molecular dynamics (SMD) simulations to derive these insights computationally. Here, we show how a key structural event at a location halfway between the RGD-binding pocket and the headpiece hinge region directly regulates hinge opening. This event is the formation of a T-junction between hydrophobic residues at the middle of the α1 helix and the top of the β6 strand and C-terminal α7 helix. This hydrophobic contact was originally identified in the description of the first open-hinge crystal structure of an integrin headpiece, that of the $\alpha_{IIb}\beta_3$ integrin (12). Here, we show that this event immedi-

---

* This work was supported by ETH Zurich, the Swiss National Supercomputing Center (CSCS, ALPS Project), and National Institutes of Health Roadmap for Medical Research Grant PN2 EY016586 to the Nanotechnology Center for Mechanics in Regenerative Medicine.

S The on-line version of this article (available at http://www.jbc.org) contains supplemental Figs. S1–S4 and Videos 1–5.

[1] Present address: Dept. of Biological Sciences, Columbia University, New York, NY 10027.

[2] To whom correspondence should be addressed. Tel.: 41-44-632-0887; Fax: 41-44-632-1073; E-mail: viola.vogel@mat.ethz.ch.

[3] The abbreviations used are: LIMBS, ligand-induced metal binding site; MIDAS, metal ion-dependent adhesion site; ADMIDAS, adjacent to the metal ion-dependent adhesion site; MD, molecular dynamics; SMD, steered molecular dynamics; N, newton.

ately precedes ligand-induced hinge opening. Vice versa, inhibition of this T-junction prevents hinge opening, and we show how Ca^{2+} at the ADMIDAS conducts this inhibitory role. In addition, we show that simulated mechanical force or "manual" opening of the hinge accelerates formation of this junction. Together with recent experimental data (10), these findings lay the groundwork for a high-resolution model of how the lifetime of the RGD-$\alpha_v\beta_3$ integrin complex can be lengthened under force, the hallmark of a "catch" bond. Differences between the βA domain model of ADMIDAS-regulated, T-junction formation described here and the pull-spring model for the structurally homologous αA integrin domain proposed elsewhere (14) are discussed.

EXPERIMENTAL PROCEDURES

System Setup—The crystal structures of the $\alpha_v\beta_3$ integrin in complex with an RGD-containing mimetic ligand (Protein Data Bank entry code 1L5G, 3.2 Å resolution (13)) and $FNIII_{10}$ from the crystal structure of the $FNIII_{7-10}$ tetramer (PDB entry code 1FNF, 2.0-Å resolution (15)) were used to build the $FNIII_{10}$-$\alpha_v\beta_3$ starting structure with the program VMD (16) as described previously (17). To reduce the integrin complex to a size that can be simulated on a feasible time scale, we used only the βA and hybrid domains of the β_3 subunit and the β-propeller domain of the α_v subunit. The starting structure was solvated in a 116 Å × 115 Å × 122 Å box of explicit TIP3 (18) water molecules, resulting in 153,570 atoms (Fig. 1*B*). For comparison, the corresponding domains from the unliganded $\alpha_v\beta_3$ integrin crystal structure (11) were also solvated in a box of explicit water molecules, resulting in 88,417 atoms. Seven cation binding sites are resolved in the crystal structure of the headpiece, three in the MIDAS, LIMBS, and ADMIDAS binding pocket motifs and four in the solvent-exposed β hairpin loops at the bottom of the α-subunit domain. These were occupied by Mn^{2+} in the crystal structure and by Mg^{2+} or Ca^{2+} in our simulations.

An additional complex was built in which the βA/hybrid domain hinge was opened "manually." To do this, the $FNIII_{10}$-$\alpha_v\beta_3$ integrin complex was aligned after 1 ns of equilibration with the same complex after 7 ns of equilibration, at which point the hinge angle had increased by ~22°. Alignment was done via the 6 β-strands of the βA domain. Once aligned, the computational coordinates of the (closed hinge) hybrid domain at 1 ns were replaced by those of the (open hinge) hybrid domain at 7 ns. In this fashion, the hinge angle of the $FNIII_{10}$-$\alpha_v\beta_3$ integrin complex, after 1 ns of equilibration, was increased manually by ~22°.

Simulation Procedures and Parameters—All MD simulations were carried out with the program NAMD (19) using the CHARMM27 force fields (20). For a detailed description of the simulation protocol, see Refs. 17 and 21. All complexes remained stable during equilibrations, exhibiting an overall Cα root mean square deviation of less than 2.0 Å in the integrin head. The integrin head is comprised of the β-propeller domain from the α_v subunit and the βA domain from the β_3 subunit.

To probe the relative kinetics of force-induced hinge angle opening, external forces were applied by SMD protocols at constant forces of 100, 150, 250, 500, 700, 800, and 900 pN (22). To examine the mechanical response of the complex in various pulling geometries, we fixed either one or both of the C-terminal residues of the integrin headpiece (*i.e.* the Cα atoms of either α_V-Arg^{438} and/or β_3-Asp^{434}). In every case, force was applied to the Cα atom at the C terminus of $FnIII_{10}$ (Thr^{93}). Generally, the direction of the stretching force was along the vector pointing from the fixed atom to the pulling atom. When the C-terminal ends of both the α and β subunits were fixed, the force vector was directed from the midpoint of the two fixed atoms to the pulling atom in the $FnIII_{10}$ domain.

Simulations were conducted on the Gonzales cluster at ETH Zürich and on the Cray XT3 Palu supercomputer at the Swiss National Computing Centre, Manno, Switzerland. A 1-ns simulation required about 24 h on 64 Dalco nodes with 2.4 GHz AMD Opteron processors, or 10 h on 64 dual core AMD Opteron nodes with 2.6 GHz processors, respectively. All structure alignments were done in VMD (22) via the backbone atoms of the 6 β-strands of the βA domain. Relative hinge angle movement was measured using a script called Hingefind (23) and the frequency of attacks by free water molecules was measured as described previously (21). Customized scripts to measure the secondary structure, the center of mass, or atom-atom distances over specific structural regions were written in Tcl within VMD. Figures were rendered using VMD.

RESULTS

Our MD and SMD approaches take advantage of the existence of the semi-equilibrated, liganded $\alpha_v\beta_3$ integrin crystal structure, which was obtained by soaking RGD-peptides into preformed, unliganded integrin crystals (13). Previously, our MD equilibrations of this structure revealed that the closed βA/hybrid domain hinge opens on the nanosecond time scale when the constraints of the bent leg domains are lifted and the RGD-ligand is replaced with the 10th type III module of fibronectin ($FnIII_{10}$, colored *yellow* in all of our figures) (17).

Here, the $FnIII_{10}$-$\alpha_v\beta_3$ integrin headpiece complex was further investigated in 25 separate simulations ranging from 3 to 7 ns each. These simulations consist of 8 MD equilibrations and 17 SMD simulations. Because Mg^{2+} is known to regulate integrin activation (8) and is present in the integrin under physiological conditions, all integrin metal ion-binding sites were occupied with Mg^{2+} unless replaced by Ca^{2+}, where specified, for comparison. The studies presented here, totaling 127 ns of simulation time, were then considered together with the 107 ns of simulation time described earlier (17).

Spontaneous Opening of the Hinge Immediately Follows Formation of a Hydrophobic T-junction between the α1 and α7 Helices—The liganded $\alpha_v\beta_3$ (11) and liganded $\alpha_{IIb}\beta_3$ (12) integrin crystal structures display a βA/hybrid domain hinge angle difference of ~62° (12, 13), a conformational change that has been linked to the switch from the inactive to the active state (2–4). However, comparison between these structures reveals near-identical configurations of the ligand-bound βA domain binding pocket, differing only in the backbone hydrogen bonding of the β1-α1 loop. In contrast, considerable variation is found between the βA domains of these structures in the region surrounding the middle of the α1 helix and the top of the C-terminal α7 helix (Fig. 1, shown *overlaid in E* and shown *separately*

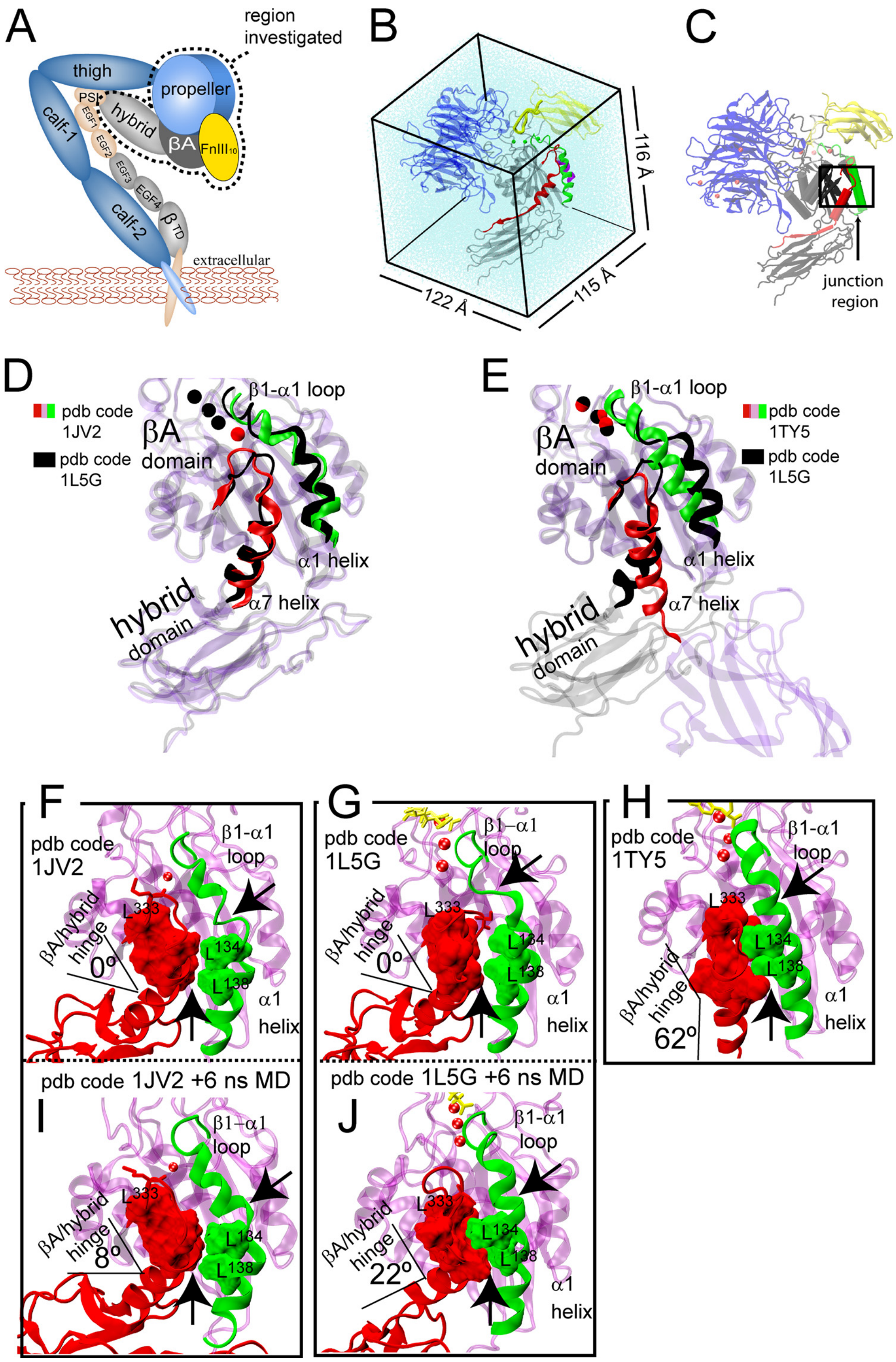

FIGURE 1. **$\alpha 1/\alpha 7$ helix T-junction formation and headpiece hinge opening are allosterically linked.** *A*, FnIII$_{10}$ (15) (*yellow*) docked to the integrin structure (13). Integrin α- and β-subunits are *blue* and *gray*, respectively. Domains not resolved in the crystal structure were added in *pink*. *B*, the headpiece complex was simulated with explicit water molecules. *C*, the region of the $\alpha 1/\alpha 7$ helix junction in the integrin headpiece is shown in the *box*. *D*, the βA and hybrid domains from the liganded $\alpha_v\beta_3$ integrin crystal structure (13), in *black*, are aligned with the same domains from the unliganded $\alpha_v\beta_3$ integrin crystal structure (11), shown in color (*red* for the $\beta 6$-$\alpha 7$ loop and $\alpha 7$ helix, *green* for the $\beta 1$-$\alpha 1$ loop and $\alpha 1$ helix, and *transparent purple* for everything else). *E*, the βA and hybrid domains from the liganded $\alpha_v\beta_3$ integrin crystal structure (13), in *black*, are aligned here with the same domains from the liganded $\alpha_{IIb}\beta_3$ integrin structure (12), shown in color. Where the hinge is closed in both structures (*D*), the greatest structural change is in the binding pocket. Where the difference in the hinge angle is ~62° (*E*), the region of greatest change is that of the $\alpha 1/\alpha 7$ T-junction. *F–H*, the three integrin crystal structures are shown separately. MD-derived snapshots (*I* and *J*) are depicted beneath the starting structures to which they correspond (*F* and *G*, respectively). The $\beta 1$-$\alpha 1$ loop/$\alpha 1$ helix and $\alpha 7$ helix/hybrid domain regions are shown in *green* and *red*, respectively. Residues of the $\beta 6$-$\alpha 7$ loop and $\alpha 7$ helix shown space-filling in *red* are Leu^{343} and Ile^{344}, located at the top of the $\alpha 7$ helix, Val^{247}, Ile^{307}, and Ala^{309}, located on underlying β-strands, and Leu^{333}, located where the $\beta 6$-strand becomes the $\beta 6$-$\alpha 7$ loop. Shown in space-filling in *green* are Leu^{134} and Leu^{138} in the $\alpha 1$ helix. *Black arrows* identify the region where the $\beta 1$-$\alpha 1$ loop meets the $\alpha 1$ helix, and the region where the $\alpha 1$ helix comes in contact with the $\beta 6$ strand and $\alpha 7$ helix during T-junction formation.

in G and *H*). Indeed, a novel hydrophobic packing in this region surrounding the middle of the $\alpha1$ helix and the top of the C-terminal $\alpha7$ helix and $\beta6$ strand was first identified in the description of the liganded $\alpha_{IIb}\beta_3$ integrin crystal structure (12) (Fig. 1*H*). Here, we report that the transition to this hydrophobic packing arrangement led to hinge opening in the RGD-occupied $\alpha_v\beta_3$ integrin headpiece. When Leu^{134}, at the middle of the $\alpha1$ helix, formed a hydrophobic junction with residues surrounding the top of the $\alpha7$ helix, the hinge increased by more than 10° over a time frame of 1 to 2 ns. This junction is evident by a tight packing between the middle of the $\alpha1$ helix and the top of the $\beta6$-strand, as shown in Fig. 1, *H* and *J* (*black arrows*). Residues of the $\alpha1$ helix and $\beta6$ strand/$\alpha7$ helix are colored *green* and *red*, respectively.

To identify T-junction formation, we measured the decrease in C_β-atom distance between the middle of the $\alpha1$ helix (Leu^{134}) and the top of the $\beta6$-strand, where it becomes the $\beta6$-$\alpha7$ loop (Leu^{333}). This distance is *traced in black* in Figs. 2, 4, and 6. Hinge opening is also displayed in supplemental Videos 1 and 2.

When the corresponding headpiece domains from the unliganded $\alpha_V\beta_3$ integrin structure were equilibrated, the hinge remained closed and the $\alpha1/\alpha7$ helix junction did not form. This is shown in the snapshot in Fig. 1*I* and the traces in Fig. 2*C*. These findings were reproduced in repeat simulations of the $FnIII_{10}$-bound and unliganded integrin headpiece domains (supplemental Fig. S1).

The difference in the $\alpha1/\alpha7$ helix junction region between the liganded $\alpha_v\beta_3$ and liganded $\alpha_{IIb}\beta_3$ structures displayed in Fig. 1*E* contrasts the close alignment of this region between the liganded and unliganded $\alpha_v\beta_3$ integrin structures displayed in Fig. 1*D*. In both the liganded and unliganded $\alpha_v\beta_3$ integrin structures, the headpiece hinge is closed and the $\alpha1/\alpha7$ helix junction is *not* formed (Fig. 1, shown *overlaid* in *D* and shown *separately in F* and *G*) (11, 13). Thus, the link between $\alpha1/\alpha7$ T-junction formation and hinge opening is consistent with crystallographic data.

Characteristic Structural Alterations That Accompany Formation of the $\alpha1/\alpha7$ Helix Junction—In the absence of the $\alpha1/\alpha7$ T-junction, a break exists in the $\alpha1$ helix. During equilibrations of the unliganded headpiece domains, this break in the $\alpha1$ helix was maintained at Asn^{133} (Fig. 3*B*). In contrast, with the junction in place, the $\beta1$-$\alpha1$ loop and $\alpha1$ helix tended to join into one continuous helix structure as shown in Fig. 1, *H* and *J*, and traced over time for residues at the center of the helix (132 to 135) in Fig. 3*A*. To quantify the fluctuations of the $\alpha1$-helix conformation, we added the number of residues in the $\beta1$-$\alpha1$ loop and $\alpha1$ helix that join in the α-helix conformation over time (residues 120 to 146). This tally is traced in *gray* in Figs. 2, 4, and 6. Another feature of $\alpha1/\alpha7$ T-junction formation is an increase in the distance between the $\beta1$-$\alpha1$ loop and the $\beta6$-$\alpha7$ loop, as shown in the *pink traces* in Figs. 2, 4, and 6.

Bidirectionality of the $\alpha1/\alpha7$ T-Junction/Hinge Opening Pathway—Experiments have shown that structural factors distal to the binding site can transition the integrin headpiece to the high affinity state by opening the βA/hybrid domain hinge (2, 4, 24). Thus, we asked if opening the hinge manually would induce the $\alpha1/\alpha7$ T-junction to form. The hinge was opened manually by replacing only the hybrid domain coordinates after 1 ns of equilibration (at which time the hinge had not yet opened), with the hybrid domain coordinates after a hinge increase of ~22°. In this fashion, a starting structure was obtained in which the $\alpha1/\alpha7$ helix junction was not in place *and* the hinge was increased by ~22°. When this complex was equilibrated in three separate simulations of 4 ns each, the $\alpha1/\alpha7$ T-junction formed within the first 40 ps in each case. As expected for a bidirectional allosteric process junction formation was accompanied by a decrease in the average Leu^{333}–Leu^{134} C_β-atom distance (Fig. 2*B*, *black trace*), an increase in the separation of the $\beta1$-$\alpha1$ and $\beta6$-$\alpha7$ loops (Fig. 2*B*, *pink trace*) and reduced fluctuations in the $\alpha1$ helix conformation (Fig. 2*B*, *gray line*).

How Ca^{2+} in Place of Mg^{2+} at the ADMIDAS Inhibits Formation of the $\alpha1/\alpha7$ T-Junction—Previously, we described 4 separate $FnIII_{10}$-$\alpha_v\beta_3$ integrin equilibrations in which small structural perturbations near the binding pocket prevented hinge opening on the nanosecond time frame (17). Here, we report that in each of these cases, hinge opening was deterred by a common mechanism: inhibition of $\alpha1/\alpha7$ T-junction formation. In one case, the structural perturbation was the replacement of Mg^{2+} with Ca^{2+} at the LIMBS and ADMIDAS in the binding pocket, which was found to promote an outwards break between the $\beta1$-$\alpha1$ loop and $\alpha1$-helix (17). Now, we report that in two separate repeat equilibrations of the Ca^{2+}-occupied complex, this outward break consistently prevailed (Fig. 3*C*) and the T-junction between the $\alpha1$ and $\alpha7$ helices did not form. Because Ca^{2+} has long been known to inhibit integrin activation (8), we asked *how* Ca^{2+} in place of Mg^{2+} promotes the split between the $\beta1$-$\alpha1$ loop and $\alpha1$-helix and thus abrogates T-junction formation.

Bidentate coordination is known to be a characteristic feature of Ca^{2+} ions, relative to Mg^{2+} (25), and this distinction was consistently displayed in all of our MD and SMD simulations (17). While the preferred number of atoms coordinating Mn^{2+} or Mg^{2+} in integrin crystal structures is six, the preferred coordination number of the Ca^{2+} ion occupying the ADMIDAS is seven (11, 12). Three of the four residues that directly coordinate the ion occupying the ADMIDAS are located along the $\beta1$-$\alpha1$ loop. These are Ser^{123}, Asp^{126}, and Asp^{127}. When Ca^{2+} occupies the ADMIDAS instead of Mn^{2+} or Mg^{2+} the seventh atom that joins the ADMIDAS coordination sphere in β_3-integrin crystal structures is the second carboxylate oxygen from Asp^{126}, located where the bottom of the $\beta1$-$\alpha1$ loop joins the top of the $\alpha1$-helix (Fig. 4*A*) (12, 13). To investigate the influence of this Ca^{2+}-specific, bidentate ADMIDAS coordination, we turned off the charge on the second Asp^{126} oxygen. In this fashion, we produced a complex in which the ADMIDAS displayed an "Mg^{2+} or Mn^{2+} mimetic" configuration while occupied by Ca^{2+}. This configuration is characterized by a single ADMIDAS-coordinating oxygen from each of the Asp^{126} and Asp^{127} $\beta1$-$\alpha1$ loop residues (Fig. 4*B*), as is the case when Mg^{2+} or Mn^{2+} occupy the ADMIDAS. Hereafter, we shall refer to this as the "Ca^{2+}-specific Asp^{126}-charge off" complex.

In three of four separate equilibrations of the Ca^{2+}-specific Asp^{126}-charge off complex (2 ns each), the 6-fold coordination of the ADMIDAS ion was maintained. In two of these simula-

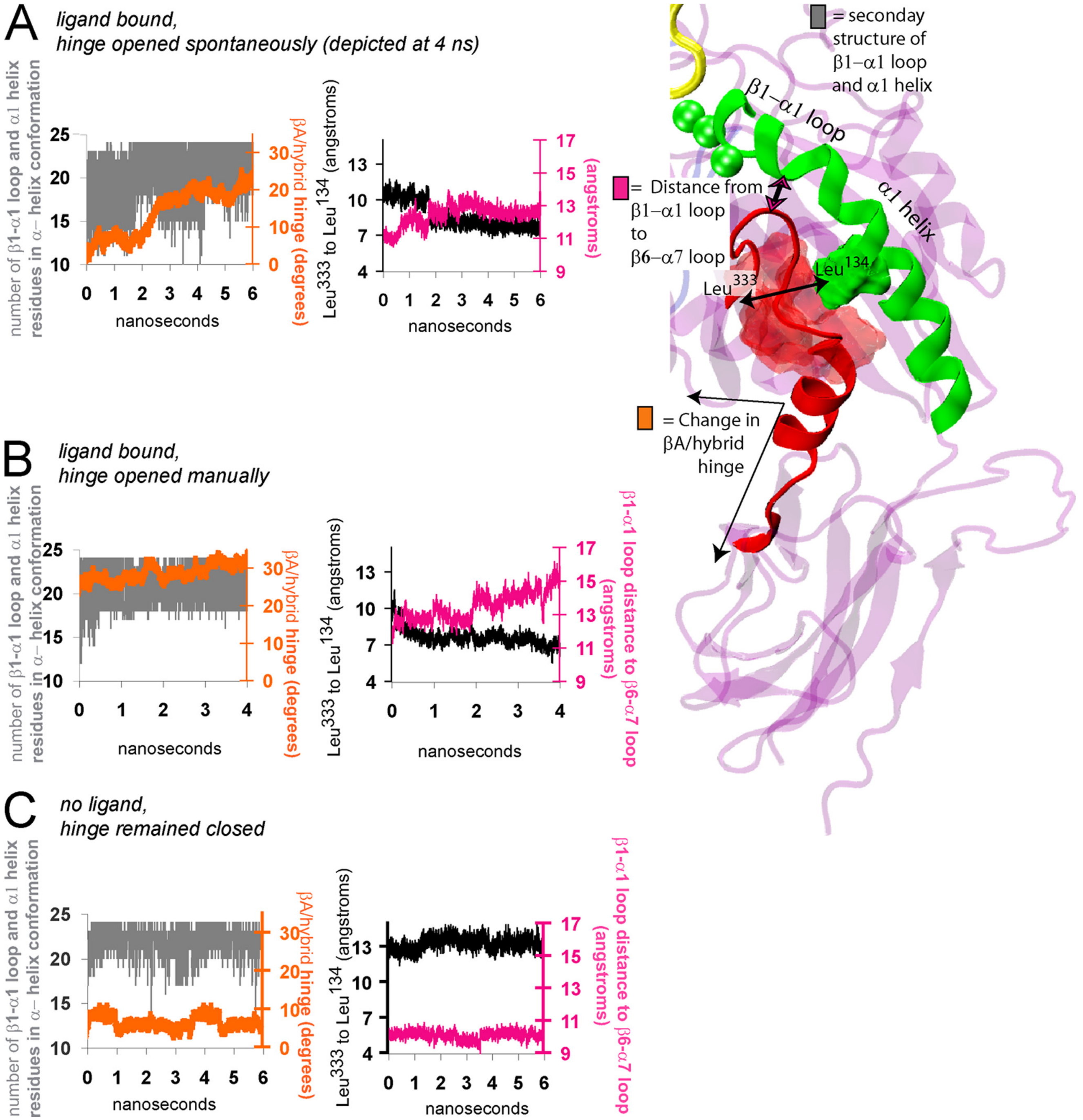

FIGURE 2. **Structural characteristics of hinge opening and $\alpha1/\alpha7$ helix T-junction formation.** Traces over the course of MD equilibrations illustrate the opening of the βA/hybrid domain hinge (*orange*), fluctuations of the $\beta1$-$\alpha1$ loop/$\alpha1$ helix (*gray*), the formation of the $\alpha1/\alpha7$ T-junction (*black*), and the distance between the $\beta1$-$\alpha1$ loop and $\beta6$-$\alpha7$ loop (*pink*). More specifically, the *orange trace* in each panel displays the relative movement of the βA and hybrid domains, the *gray trace* in each panel displays the number of residues across the $\beta1$-$\alpha1$ loop and $\alpha1$ helix (residues 120 to 146) that form an α helix over time, the *black trace* in each panel is the C_{β}-atom distance between Leu^{134} of the $\alpha1$ helix and Leu^{333} on the $\beta6$ strand, and the *pink trace* in each panel is the distance between the centers of mass of the $\beta1$-$\alpha1$ loop (residues 122 to 127) and the $\beta6$-$\alpha7$ loop (residues 333 to 340). To obtain the number of residues across the $\beta1$-$\alpha1$ loop and $\alpha1$ helix that form an α helix over time (*gray trace*), each of the 26 residues is assigned either a "1" or "0," corresponding to whether the residue was participating in an α helix (*1*) or not (*0*). Then these numbers were summed and traced over time. The maximum value of this measurement was 24, because Leu^{120} and Ser^{121}, located at the *top* of the $\beta1$-strand, do not ever join the α helix. During spontaneous hinge opening (*A*, *orange trace*), the $\beta1$-$\alpha1$ loop and $\alpha1$ helix fluctuations displayed a wide range (*A*, *gray trace*). The $\alpha1/\alpha7$ T-junction formed when the hinge opened spontaneously (*A*, *black trace*) or manually (*B*, *black trace*). The α helix fluctuations were relatively less when the hinge was opened manually (*B*, *orange* and *gray traces*) or remained closed (*C*, *orange* and *gray traces*). When the hinge remained closed, the $\alpha1/\alpha7$ T-junction did not form (*C*, *black trace*). A characteristic of the $\beta1$-$\alpha1$ loop that accompanies $\alpha1/\alpha7$ T-junction formation is an increased separation from the $\beta6$-$\alpha7$ loop (*pink trace*, *A* and *B versus C*). To view repeat simulations with the same analysis, see supplemental Fig. S1.

tions, the $\alpha1/\alpha7$ T-junction formed. In both of these cases, the most prevalent conformation of the $\beta1$-$\alpha1$ loop and $\alpha1$-helix switched from that of the split conformation that is typical of Ca^{2+} occupation (Fig. 4*A*) to the continuous helix conformation that we otherwise found in Mg^{2+}-occupied complexes (Fig. 4*B*). In the third simulation, a hydrogen bond between the top of the α1-helix (at Trp^{129}) and the β6-α7 loop (at Ser^{338}) remained formed, which caused the split between the β1-α1 loop and α1-helix to remain in place. In the fourth simulation, 7-fold coordination of the Ca^{2+}-occupied ADMIDAS was restored when the second carboxylate oxygen from Asp^{127}, instead of Asp^{126}, joined the Ca^{2+} coordination sphere. Strikingly, in this case the split between the β1-α1 loop and α1-helix became exaggerated, relative to the split configuration that is typical of "wild-type" Ca^{2+}-occupied complexes (supplemental Fig. S2).

Together with experimental evidence linking Ca^{2+} at the ADMIDAS with integrin activation inhibition (26) and mutations of the ADMIDAS with changes in the headpiece hinge angle (27), these simulations suggest that the structural basis for activation inhibition by Ca^{2+} is as follows: Ca^{2+} at the ADMIDAS promotes bidentate coordination by a β1-α1 loop Asp, which in turn favors the outwards split between the β1-α1 loop and α1-helix, which in turn hinders α1/α7 helix junction formation, which obstructs hinge opening (Fig. 5).

Force Accelerates Formation of the α1/α7 Helix T-Junction—Previously, we used SMD simulations to show that tensile force accelerates the opening of the integrin headpiece hinge (17). Here, we asked if force also accelerates the formation of the T-junction between the α1 and α7 helices. In nine separate SMD simulations, force was applied to the Mg^{2+}-occupied integrin complex after 1 ns of equilibration, at which point the α1/α7 T-junction was not yet formed and the hinge was still closed. Forces of 100 to 900 pN were applied via the C terminus of the $FnIII_{10}$ module. Forces in the hundreds of piconewtons were chosen to observe structural changes over a computationally feasible time frame. To vary the direction of strain, force was applied with the C terminus of only the hybrid domain fixed (at 100, 150, and 250 pN) or

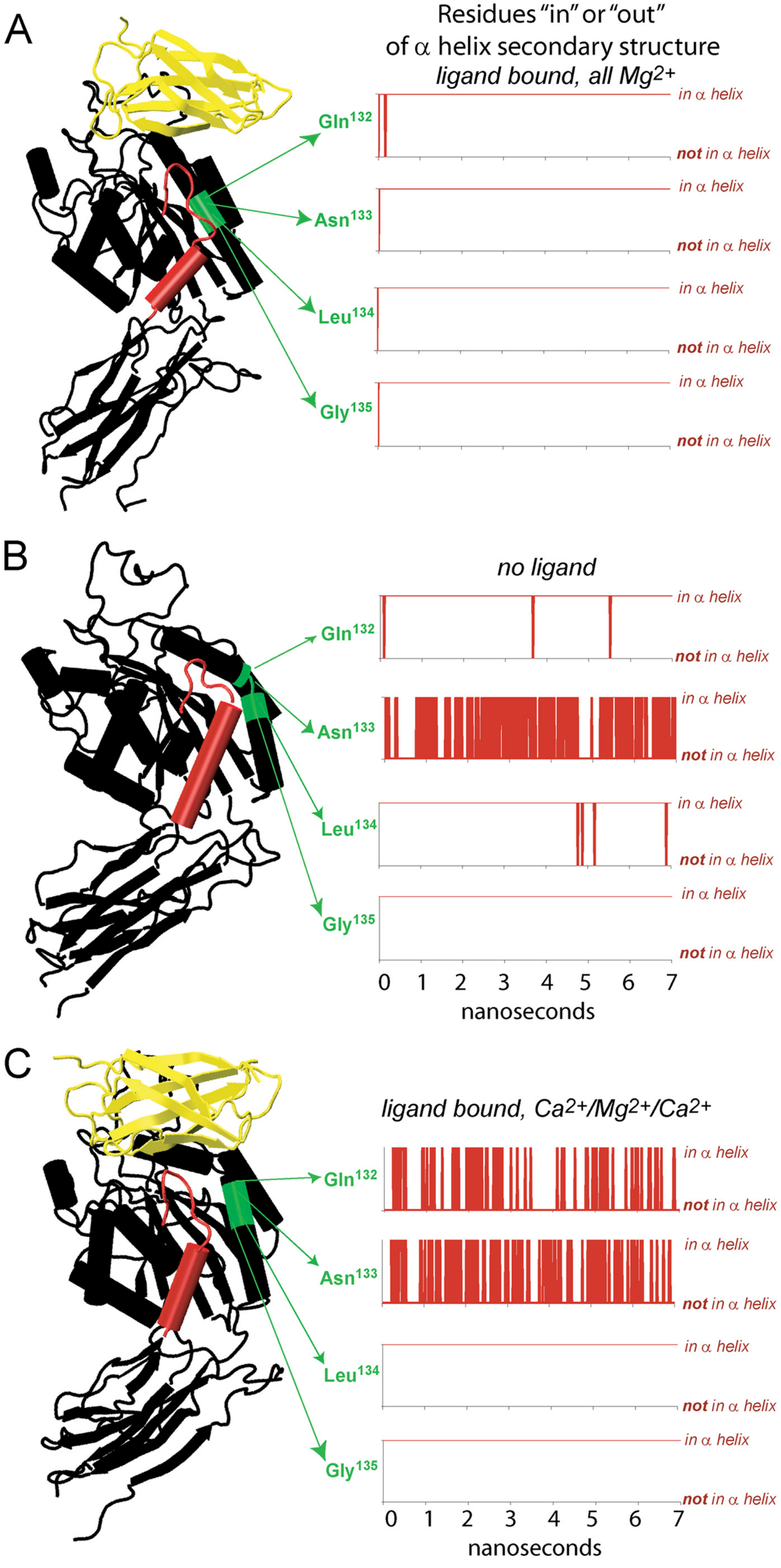

with the C termini of both the α subunit β-propeller domain and the hybrid domain fixed (at 500, 700, 800, and 900 pN).

We found that force induced the $\alpha1/\alpha7$ T-junction to form within the 5-ns time frame in seven (of nine) simulations. These include two in which the hinge was free to open under force and five in which the closed hinge was constrained. Even in the latter case, force varied the constrained hinge angle by as much as 15°. For representative depictions, see Fig. 6 and supplemental Videos 3 and 4.

We found that force could induce the T-junction to form prior to inducing a significant change in the hinge angle. This is illustrated in Fig. 6 by the decrease in the Leu^{333}–Leu^{134} C$_\beta$-atom distance (*black trace*) that occurs prior to the corresponding hinge increase (*orange trace*). When the $\alpha1/\alpha7$ T-junction did not form under force (two of nine times) the split between the $\beta1$-$\alpha1$ loop and the $\alpha1$ helix displayed greater prevalence and the $\beta1$-$\alpha1$ loop and $\beta6$-$\alpha7$ loop remained in close proximity (supplemental Video 5, in contrast to supplemental Videos 3 and 4).

Once the $\alpha1/\alpha7$ T-junction was formed in a mechanically strained integrin complex, it remained stable (seven simulations). In three additional simulations, forces of 500, 800, and 900 pN were applied for several nanoseconds after the junction was formed. Even at these high pulling forces, the junction was not disrupted.

Next, we asked if force could induce formation of the $\alpha1/\alpha7$ T-junction in Ca^{2+}-occupied complexes, because we did not observe this event under equilibrium conditions (three of three Ca^{2+}-occupied equilibrations). When the hinge of Ca^{2+}-occupied complexes was opened under forces of 100, 150,

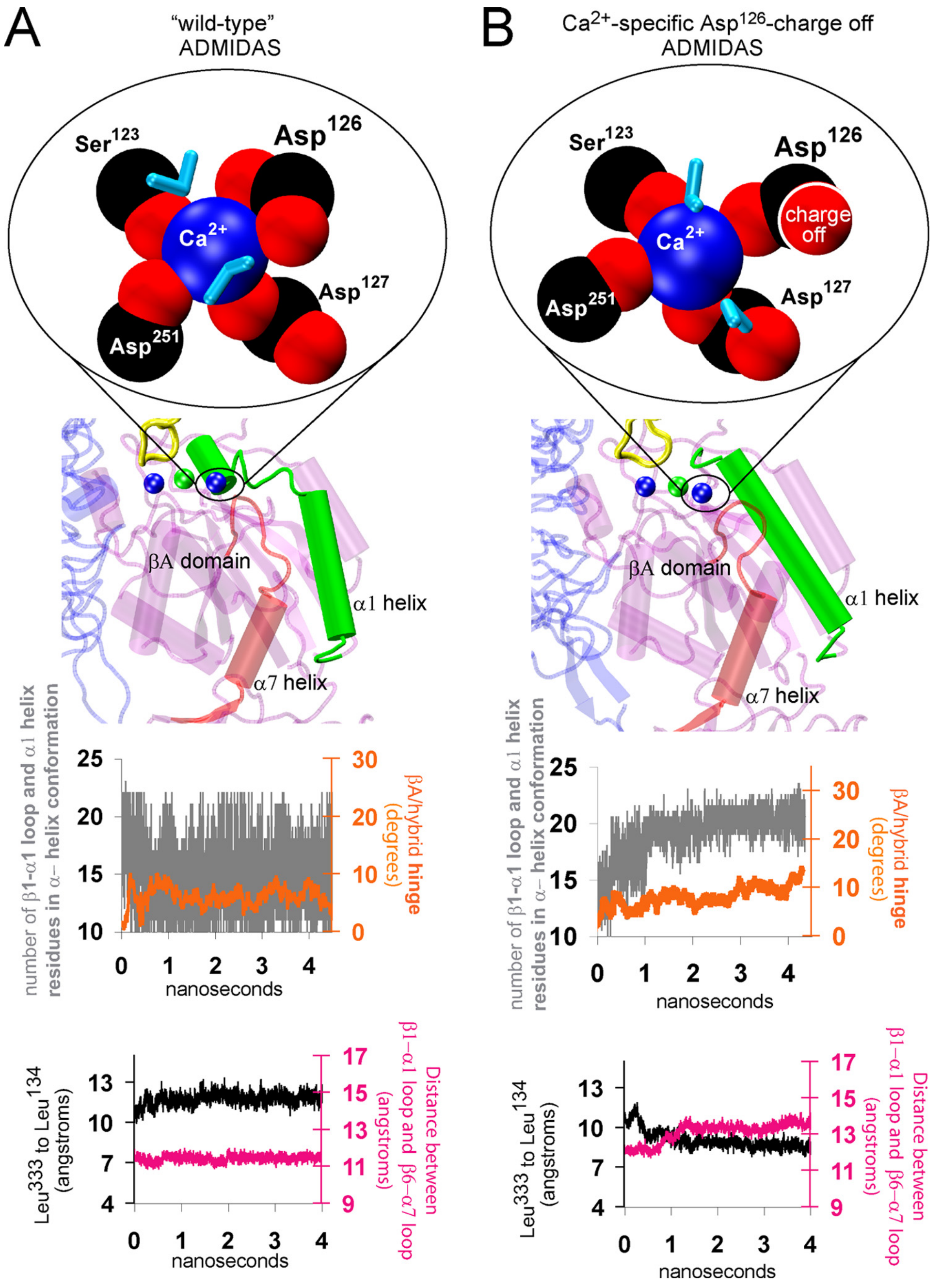

FIGURE 4. **How Ca^{2+} in place of Mg^{2+} at the ADMIDAS inhibits formation of the $\alpha1/\alpha7$ helix T-junction.** *A*, *top*, the coordination shell of the Ca^{2+}-occupied ADMIDAS. Water molecules are shown in *cyan* licorice representation. When Ca^{2+} replaces Mg^{2+}, the second carboxyl oxygen from Asp^{126} joins the coordination sphere and a split becomes more prevalent between the $\beta1$-$\alpha1$ loop and $\alpha1$ helix (see Fig. 3*C*). Under equilibrium conditions, the hinge does not open on the nanosecond time scale and the $\alpha1/\alpha7$ T-junction does not form in Ca^{2+}-occupied complexes (compare with Fig. 2*A*). *B*, when the charge on the second Asp^{126} oxygen was turned off, in Ca^{2+}-occupied complexes, creating a Ca^{2+}-specific Asp^{126}-charge off complex, the most prevalent conformation of the $\beta1$-$\alpha1$ loop and $\alpha1$ helix switched to an uninterrupted helical structure. Also, the $\alpha1/\alpha7$ T-junction formed (*bottom*, *black trace*) and a greater increase is evident in the hinge (*middle*, *orange trace*). When force was applied to this Ca^{2+}-specific Asp^{126}-charge off complex, hinge opening was accelerated relative to Ca^{2+}-occupied complexes (supplemental Fig. S3). For further depiction of how the bidentate ADMIDAS coordination governs the $\beta1$-$\alpha1$ loop conformation, see supplemental Fig. S2.

FIGURE 3. **The $\alpha1$ helix split.** The helical conformation of the middle of the $\alpha1$ helix (residues 132 to 135) was assessed by residues over time using the "ssrecalc" command in VMD. *A*, when the hinge opened spontaneously, all of these residues were maintained in the α helix conformation. *B*, in the unliganded structure, Asn^{133} fluctuated in and out of the α helix conformation, resulting in a split helix. *C*, when Ca^{2+} replaced Mg^{2+} at the LIMBS and ADMIDAS, Gln^{132} and Asn^{133} fluctuated in and out of the α helix conformation, again resulting in a split helix. In all of our simulations, we found the prevalence of the split $\alpha1$ helix to be a characteristic feature of complexes in which the hinge did not open on the nanosecond time scale (*e.g.* unliganded or Ca^{2+}-occupied complexes).

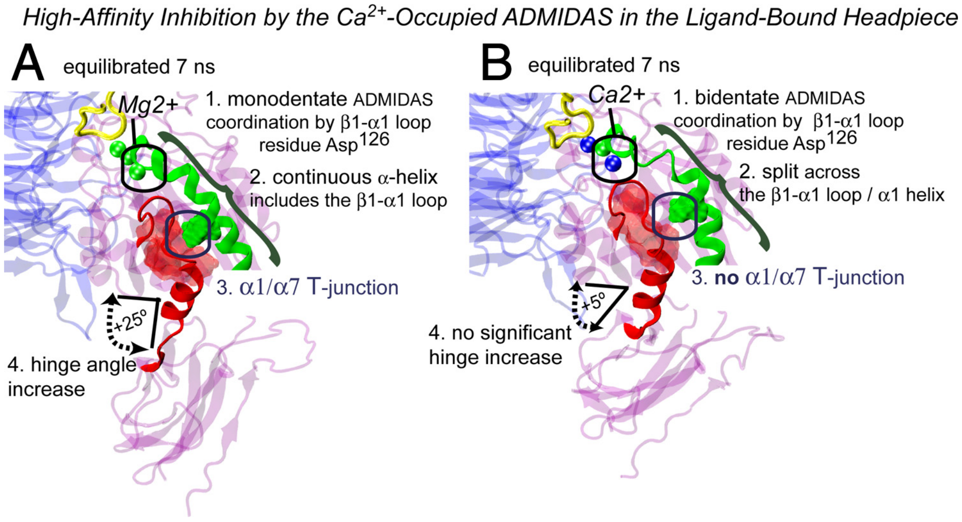

FIGURE 5. **Model of the structural pathway across the βA domain by which Ca^{2+} in place of Mg^{2+} at the ADMIDAS in the ligand-bound headpiece inhibits βA/hybrid domain hinge angle opening.** The RGD loop from $FnIII_{10}$ is visible in *yellow* and the α-subunit domain is visible in *blue*. *A*, with Mg^{2+} occupying the ADMIDAS of the ligand-bound headpiece, monodentate coordination by the $\beta1$-$\alpha1$ loop aspartates promotes the uninterrupted conformation of the $\alpha1$ helix and thus $\alpha1/\alpha7$ T-junction formation and hinge angle opening. *B*, with Ca^{2+} occupying the ADMIDAS in the ligand-bound headpiece, bidentate coordination by a $\beta1$-$\alpha1$ loop aspartate promotes the split conformation of the $\alpha1$ helix, which hinders $\alpha1/\alpha7$ T-junction formation and hinge angle opening.

and 250 pN, according to the same protocol described above for Mg^{2+}-occupied complexes, formation of the $\alpha1/\alpha7$ T-junction accompanied hinge opening two of three times (at 100 and 250 pN).

Hinge opening in Ca^{2+}-occupied complexes occurred with a delay relative to Mg^{2+}-occupied complexes. Thus, we asked if the same structural feature regulates hinge opening and $\alpha1/\alpha7$ T-junction formation under force that we found to regulate this pathway under equilibrium conditions: namely, the $\beta1$-$\alpha1$ loop/ADMIDAS coordination. We found that when the same constant forces were applied to the Ca^{2+}-specific Asp^{126}-charge off complex, force-induced hinge opening was accelerated toward the time scale of Mg^{2+}-occupied complexes (supplemental Fig. S3). In other words, like ligand-induced hinge opening, force-accelerated hinge opening was found to be regulated by the influence of the bidentate $\beta1$-$\alpha1$ loop ADMIDAS coordination.

Alterations of the $\beta1$-$\alpha1$ Loop Shield the Force-bearing RGD-Integrin Bond from Water Access—Having established a link between $\beta1$-$\alpha1$ loop contacts and the $\alpha1/\alpha7$ T-junction, we next asked if the $\beta1$-$\alpha1$ loop could regulate the lifetime of the principal RGD-$\alpha_v\beta_3$ integrin bond. Previous SMD studies have shown that force-bearing bonds break when free water molecules compete with the bonding partners to form hydrogen bonds (21, 28). This indicates that the lifetime of a force-bearing bond can be increased by small structural perturbations that lessen access of free water to the bond. In the $\alpha_v\beta_3$ integrin complex, the principal force-bearing bond occurs between a carboxyl oxygen on Asp^{RGD} and the MIDAS ion (21). Thus, we investigated whether the $\beta1$-$\alpha1$ loop can regulate access of free water molecules to this bond.

The top of the $\beta1$-$\alpha1$ loop packs flush against the force-bearing Asp^{RGD}-MIDAS ion bond via direct contacts with both the MIDAS ion and Asp^{RGD} (Fig. 7*A*). The contact with Asp^{RGD} involves the "second" carboxyl oxygen (*i.e.* the Asp^{RGD} side chain oxygen that is not bound to the MIDAS ion) and Tyr^{122}. In our simulations, we found that this contact was sometimes lost in Mg^{2+}-occupied complexes when the second Asp^{RGD} side chain oxygen joined the first in coordinating the MIDAS ion (Fig. 7*D*). Although formation of the bidentate MIDAS ion coordination by Asp^{RGD} may not be physiologically relevant, as it is not currently found in crystal structures, we used this structural event to compare the influence of the Asp^{RGD}–Tyr^{122} bond on the access of water molecules to the force-bearing Asp^{RGD}–MIDAS ion bond.

Analysis of the number of collision events between free water molecules and the MIDAS ion-coordinating Asp^{RGD} oxygen (Oδ-2) reveals a considerable shielding when the Asp^{RGD}–Tyr^{122} bond is in place (Fig. 7, *C versus E*). During SMD simulations begun with the bidentate Asp^{RGD}-MIDAS ion coordination in place, it either remained formed (six of nine) or switched to monodentate Asp^{RGD}-MIDAS ion coordination together with Asp^{RGD}–Tyr^{122} bond formation (three of nine). In the latter cases, we found that the frequency of water attacks on the ion-coordinating Asp^{RGD} oxygen decreased when the Asp^{RGD}–Tyr^{122} bond was formed, as illustrated in Fig. 7*B*. These findings suggest a critical role for the Asp^{RGD}–Tyr^{122} bond, and thus of the $\beta1$-$\alpha1$ loop, in regulating the lifetime of the principal RGD–$\alpha_v\beta_3$ integrin bond.

DISCUSSION

Although experiments have linked the switch to high affinity binding in the integrin headpiece with the opening of the βA/hybrid domain hinge (2–4), the structural basis for this link has remained unclear. On the one hand, the first crystal structure of the ligand-bound integrin headpiece (13) was formed under conformational constraints (17) and displays a closed βA/hybrid domain hinge. On the other hand, this crystal structure displays a conformation of the ligand-bound binding pocket that is nearly identical to that of the open-hinge β_3 integrin headpiece structure, which was solved subsequently by co-crystallization with ligand (12). Thus, these crystallographic snapshots beg the question of *how* the conformation of the βA/hybrid domain hinge governs structural events in the vicinity of the βA domain binding pocket.

The simulations presented here were based on a semi-equilibrated crystal structure, in which activating structural changes local to the binding pocket had already occurred as a result of ligand binding but long-range propagation of the activation signal had been arrested by domain-domain contacts in the pre-existing crystal lattice. Previously, we showed with molecular dynamics simulations based on this structure that a small inwards (*versus* outwards) movement of the $\alpha1$ helix promotes

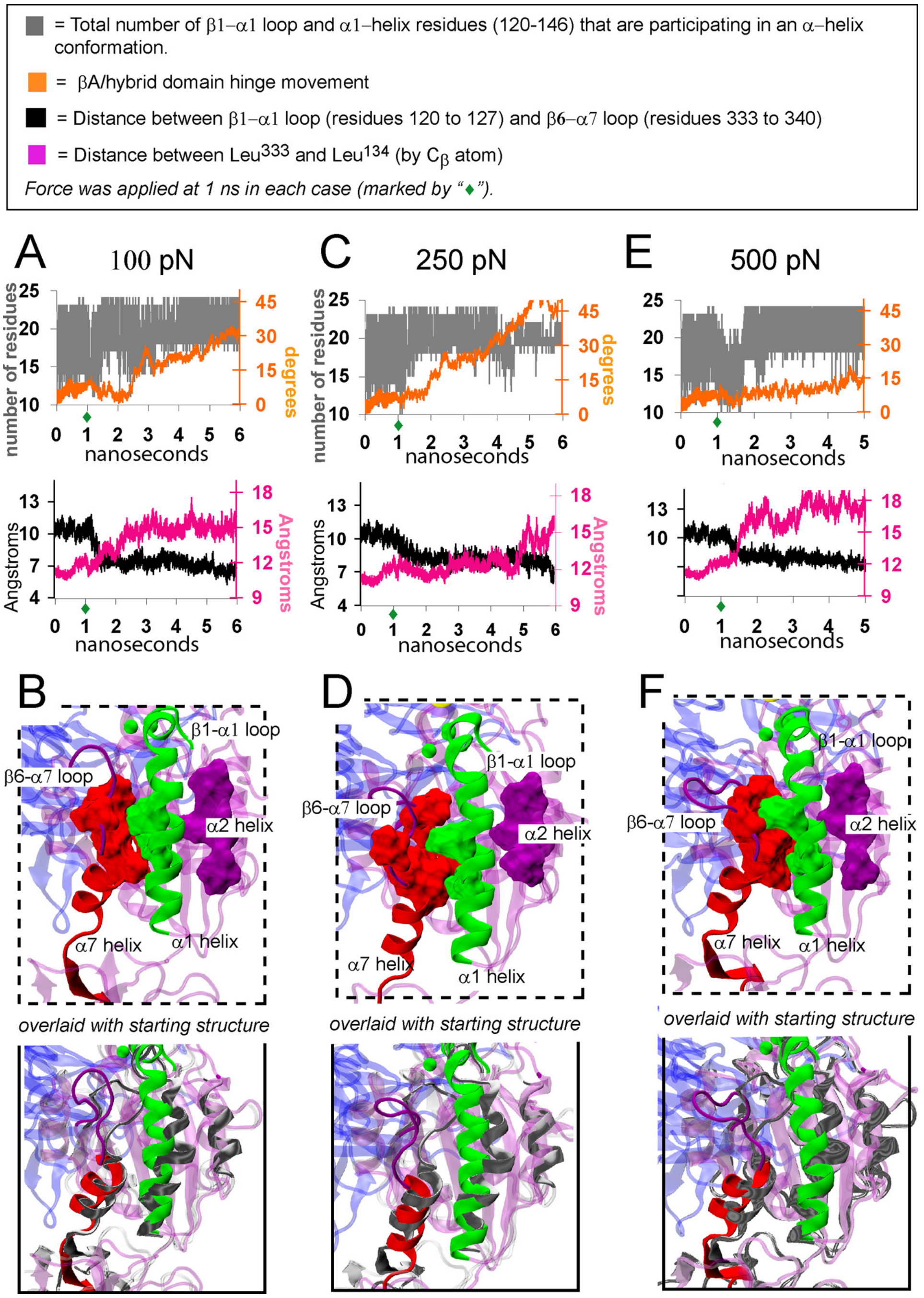

FIGURE 6. **Force-induced α1/α7 helix junction formation.** Traces from three separate SMD simulations are shown, with corresponding structural snapshots beneath. In each case, force was applied to FnIII$_{10}$ after 1 ns of equilibration and was found to induce α1/α7 T-junction formation. Force was applied to the C terminus of the FnIII$_{10}$ module with the C terminus of the β hybrid domain fixed. When force was applied at 500 pN (*E* and *F*), opening of the hinge angle was constrained by also fixing the C terminus of the α subunit β propeller domain. All snapshots are from the 3rd ns under force. In the *bottom panels*, each snapshot is overlaid with the starting crystal structure (shown in *gray*).

(*versus* impedes) opening of the βA/hybrid domain hinge (17). Here, we have shown how a contact of the α1 helix that occurs approximately halfway between the RGD-binding pocket and the βA/hybrid domain hinge links the signal propagation between these two sites. This contact is an α1/α7 T-junction between hydrophobic amino acid side chains in the middle of the α1-helix, the top of the β6-strand, and the top of the C-terminal α7-helix. We found that formation of this junction results from RGD occupation of the binding pocket and, as expected for allosterically regulated proteins, can also be induced by βA/hybrid domain hinge opening. A characteristic of this α1/α7 T-junction is the fusion of the α1-helix and β1-α1 loop, resulting in one continuous helix structure flanking the side of the βA domain (Figs. 1, *H* and *J*, and 3*A*). A change in ADMIDAS ion coordination, resulting from Ca^{2+} in place of Mg^{2+}, inhibits formation of the α1/α7 T-junction by stabilizing a break between the β1-α1 loop and the α1-helix (Figs. 3*C* and 4*A*). Mechanical force was found to accelerate formation of the α1/α7 T-junction (Fig. 6). Taken in consideration with mutational, monoclonal antibody, electron micrographic and tomographic experiments that link the βA/hybrid domain hinge opening with integrin activation (2–4), together with recent evidence of force-accelerated integrin activation (9, 10), formation of the α1/α7 T-junction appears to be a key event along the integrin activation pathway.

Recently, five activating point mutations have been identified in the β-subunit headpiece domain (29). A preliminary analysis of the solvent accessible surface areas of these residues in our simulations indicates changes before and after α1/α7 T-junction formation that are consistent with the model proposed here. These include decreased fluctuations in residues located close to junction formation on the α1 and α2 helices and increased fluctuations in residues located at the βA/hybrid domain interface.[4]

Residues of the α1/α7 Helix T-junction Are Highly Conserved—The hydrophobic α1/α7 T-junction residues Leu^{138}, Leu^{333}, Leu^{343}, Val^{247}, Ile^{307}, and Ala^{309} are completely conserved across the 8 integrin β-subunits, whereas Leu^{134} and Ile^{344} are conserved across 6 β-subunits. These residues are shown in *green* and *red* surface representations in Figs. 1 and 6. In the integrin β$_8$A domain, both Leu^{134} and Ile^{344} are replaced by the similarly

---

[4] E. Puklin-Faucher and V. Vogel, unpublished data.

hydrophobic Val, whereas in the β_4A domain, they are replaced by hydrophobic residues Met and Leu, respectively.

In accord with the premise of the model described here for the $\alpha_v\beta_3$ integrin, experiments have shown that mutations of hydrophobic residues on the $\alpha1$ and $\alpha7$ helices influence activation of the $\alpha_5\beta_1$ integrin as well (30). Although the key residues identified experimentally differ from the $\alpha1/\alpha7$ T-junction residues identified here, there is a large degree of hydrophobic redundancy across highly conserved residues of the $\alpha1$- and $\alpha7$-helices (supplemental Fig. S4). For example in a preliminary study, we found that when Leu^{131}, located above Leu^{134} in the $\alpha1$ helix, is computationally "mutated" to Ala that a different kind of $\alpha1/\alpha7$ T-junction formed. In this case, a hydrophobic residue from the top of the $\alpha7$ helix, Ile^{344}, became inserted into a hydrophobic pocket in the $\alpha1$ helix between Leu^{138} and Met^{142} and the headpiece hinge angle displayed an increase of ~20° after 5 ns of equilibration (data not shown). Experimentally mutating the equivalent Leu residue in the $\alpha_5\beta_1$ integrin was shown to promote activation (30). Thus, we suggest that a variety of putative hydrophobic interactions between the $\alpha1$ and $\alpha7$ helices could influence the dynamics of the $\beta1$-$\alpha1$ loop and thereby influence binding affinity of the RGD-binding pocket.

A Unique Role for the ADMIDAS in βA Domain Allostery—Although all 24 known integrin heterodimers include the three headpiece domains investigated here, 9 types of integrins additionally contain the αA domain (also called the I domain) inserted into the extracellular end of the α-subunit. In those integrins that contain it, the αA domain mediates ligand binding directly. Although the αA and βA domains share considerable functional and structural homology, our simulations indicate that their mechanisms of activation differ. Although αA domain activation has been shown to proceed via the ratchet-like movement of the $\beta6$-$\alpha7$ loop through an underlying pocket of the hydrophobic protein core (31), βA domain activation involves a distinctive, key role for the $\alpha1$ helix and the ADMIDAS, a metal ion binding site that is not present in the αA domain (17, 26). Our simulations indicate that the change in bidentate ADMIDAS coordination that accompanies the change in occupation from Mg^{2+} or Mn^{2+} to Ca^{2+} regulates βA domain activation via an influence on $\alpha1/\alpha7$ T-junction formation.

Recent mutational studies of the $\beta1$-$\alpha1$ loop ADMIDAS coordinating residues have shown disparate effects on integrin binding affinity. In one case, mutations equivalent to Asp^{126} induced firm adhesion in flow chamber experiments of $\alpha_4\beta_7$ integrins (32). In the other case, the corresponding mutation induced weakened adhesion in solid phase binding assays of

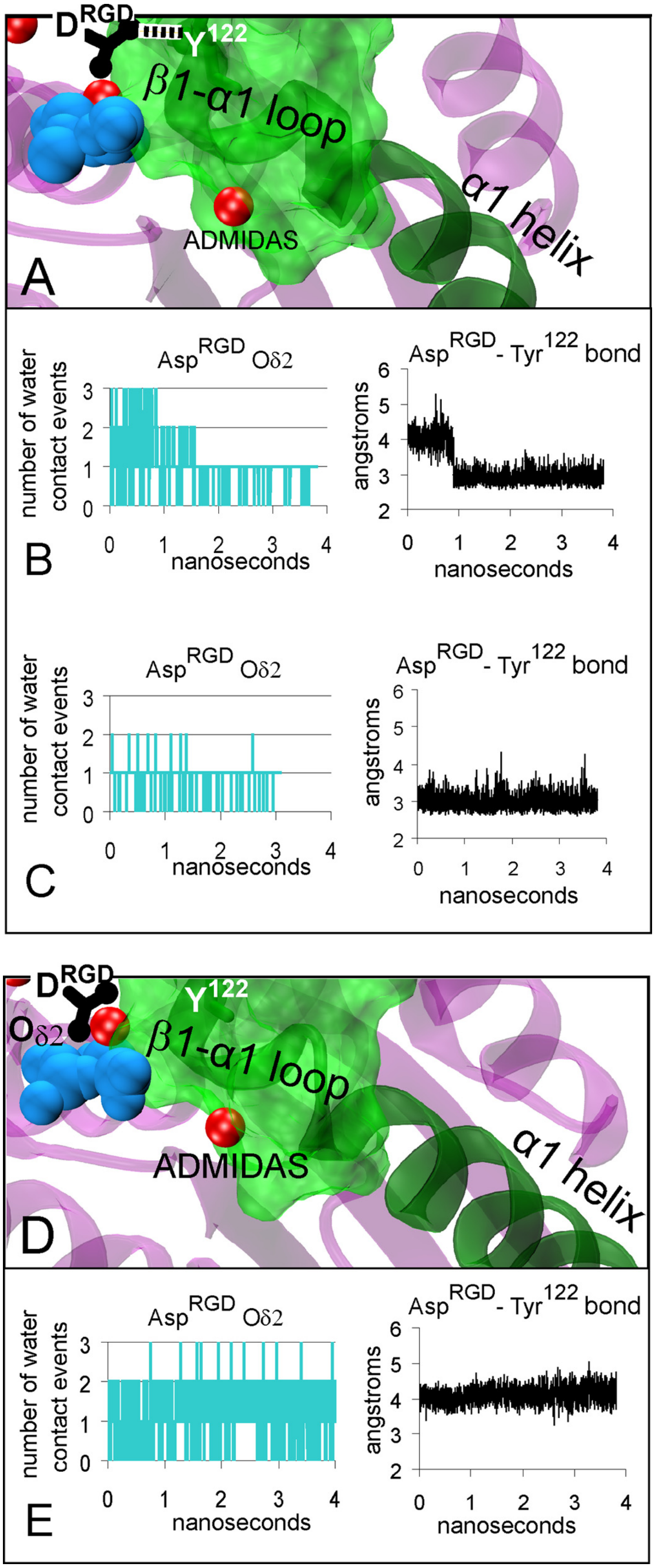

FIGURE 7. **The $\beta1$-$\alpha1$ loop regulates the stability of the force-bearing Asp^{RGD}-MIDAS bond.** *A*, the force-bearing bond between Oδ-2 of Asp^{RGD} (*black*) and the MIDAS ion (*red*) occurs at the *top* of the $\beta1$-$\alpha1$ loop, shown in *green*, *schematic,* and *transparent surface* representations. When the Asp^{RGD} and Tyr^{122} hydrogen bond is formed (*dashed line*), the $\beta1$-$\alpha1$ loop packs in tightly with the Asp^{RGD} side chain. Water molecules within 5 Å of the Oδ-2 atom are shown in *blue* van der Waals representation. *B*, when the bond between Asp^{RGD}–Tyr^{122} was formed under force, as evident from the trace of the heavy atom distance (*right side*, traced in *black*), shielding of force-bearing Oδ-2 atom from attack by free water molecules was increased (*left side*, traced in *blue*). Water contact events to the Oδ-2 atom were counted for each time step (picosecond intervals) by identifying the number of water molecules within 3 Å of the Oδ-2 atom. *C*, when the Asp^{RGD}–Tyr^{122} bond was already formed under force, this bond remained formed (*right side*, *black* trace) and the Oδ-2 atom remained shielded from attack by water molecules (*left side*, *blue* trace). When instead both of the Oδ-1 and Oδ-2 atoms coordinated the MIDAS ion (*D*) and the Asp^{RGD}–Tyr^{122} bond did not form (*E*, *right side*), the Asp^{RGD} atom that forms the force-bearing bond with the MIDAS ion, Oδ-2, was subject to a relatively higher level of water molecule attacks.

$\alpha_5\beta_1$ (33) and $\alpha_2\beta_1$ integrins (27). In this case, mutationally induced activation inhibition was partially rescued by monoclonal antibodies 12G10 or TS2/16, which bind at or near the α1 helix (2, 26). In all cases, ADMIDAS was found to play a critical role in relaying allostery from the ligand binding pocket to the rest of the integrin molecule. Notably, cell rolling assays probe integrin binding under tensile force conditions imposed by fluid flow, whereas solid phase binding assays probe integrin binding interactions in the absence of tensile forces. Thus, these seemingly disparate findings are also consistent with the model described here, whereby we predict that force applied to Ca^{2+}-occupied complexes could override the α1 helix split that otherwise occurs, allowing the $\alpha1/\alpha7$ T-junction to form. In other words, this is how force could reverse the inhibitory influence of the Ca^{2+}-occupied ADMIDAS. It should also be pointed out that ADMIDAS residues are completely conserved across all integrin β subunits except the β_8 subunit, where the two $\beta1$-$\alpha1$ loop/α1 helix aspartates are replaced by similarly acidic asparagines.

Force-accelerated Allostery and the Integrin Catch Bond—Several receptor-ligand complexes have been shown to increase their binding affinity under force, the hallmark of a catch bond. These include the bacterial adhesin FimH with mannose (34), the myosin-actin motor protein complex (35), the cellular adhesins P- and L-selectin with their respective ligands (36, 37) and, most recently, the $\alpha_5\beta_1$ integrin with $FnIII_{7-10}$ (10). In each case, a structural change has been implicated that is first induced or accelerated by force and then extends the lifetime of the receptor-ligand bond (for reviews, see Refs. 38–40). Like integrins, the FimH ligand binding site is allosterically coupled to a distal hinge region (40). Also like integrin catch bond complexes, activation of the FimH and selectin catch bond complexes can be stabilized by point mutations or monoclonal antibodies that promote the opening of the headpiece hinge, even if their epitopes are located distal to the ligand-binding site. Yet, for each of the receptor-ligand catch bond complexes currently known, the structural changes in the binding pocket that enable the extension of the bond lifetime remain experimentally undetermined (36, 41).

Here, we have shown that in the case of the RGD-$\alpha_v\beta_3$ integrin complex, formation of a bond between the $\beta1$-$\alpha1$ loop (Tyr^{122}) and Asp^{RGD} will extend the lifetime of the principal RGD-integrin bond by shielding it from frequent attacks by free water molecules (Fig. 6). This finding is consistent with available pharmacophoric refinement data, which identified the same bond as critical for RGD-integrin binding stability (42). It is also consistent with a general mechanism for allosteric proteins, whereby the dual character of regions of low and high structural stability in the binding site leads to the propagation of structural change via the region of low structural stability (43). In accord with this general mechanism, the $\beta1$-$\alpha1$ loop both connects directly to the $\alpha1/\alpha7$ T-junction and, as shown in comparison across crystal structures of various presumed affinities (Fig. 1, *D–H*), is the only loop in the immediate vicinity of the Asp^{RGD}-MIDAS ion bond that displays significant structural change. This model is also consistent with the recent finding that monoclonal antibodies that activate integrins by their influence on the α1 helix also shift the integrin catch bond to a lower force regime (10).

As evidenced in crystallographic data (12, 13), formation of the $\alpha1/\alpha7$ T-junction occurs only once the βA domain is free to re-equilibrate after a binding event. Equilibration of the βA domain might be hindered by domain-domain contacts such as those formed in the bent-knee conformation of inactivated integrins. Although the two available liganded crystal structures display near identical configurations of the liganded β_3 integrin binding pocket, differing only in backbone hydrogen bonding of the $\beta1$-$\alpha1$ loop, the $\alpha1/\alpha7$ T-junction is absent where the ligand was soaked into preformed integrin crystals (13) that where constrained in the closed-hinge conformation by the pre-existing crystal lattice (17). In contrast, the junction is formed where the ligand was co-crystallized with the integrin headpiece in the absence of the legs domains (12). Thus, we propose that the physiological role of the bent-knee conformation is to tune, by domain-domain contact, the height of the energy barrier necessary to transition the headpiece to the high affinity state via hinge opening and $\alpha1/\alpha7$ T-junction formation. This may be the mechanism by which force accelerates the integrin activation process.

Acknowledgments—We gratefully acknowledge Drs. M. Gao, M. Smith, and V. Hytönen and Profs. K. Schulten and M. P. Sheetz for discussions.

REFERENCES

1. Hynes, R. O. (2002) *Cell* **110,** 673–687
2. Mould, A. P., Barton, S. J., Askari, J. A., McEwan, P. A., Buckley, P. A., Craig, S. E., and Humphries, M. J. (2003) *J. Biol. Chem.* **278,** 17028–17035
3. Luo, B. H., Strokovich, K., Walz, T., Springer, T. A., and Takagi, J. (2004) *J. Biol. Chem.* **279,** 27466–27471
4. Luo, B. H., Springer, T. A., and Takagi, J. (2003) *Proc. Natl. Acad. Sci. U.S.A.* **100,** 2403–2408
5. Wegener, K. L., Partridge, A. W., Han, J., Pickford, A. R., Liddington, R. C., Ginsberg, M. H., and Campbell, I. D. (2007) *Cell* **128,** 171–182
6. Arnaout, M. A., Mahalingam, B., and Xiong, J. P. (2005) *Annu. Rev. Cell Dev. Biol.* **21,** 381–410
7. Takagi, J., Strokovich, K., Springer, T. A., and Walz, T. (2003) *EMBO J.* **22,** 4607–4615
8. Mould, A. P., Akiyama, S. K., and Humphries, M. J. (1995) *J. Biol. Chem.* **270,** 26270–26277
9. Friedland, J. C., Lee, M. H., and Boettiger, D. (2009) *Science* **323,** 642–644
10. Kong, F., García, A. J., Mould, A. P., Humphries, M. J., and Zhu, C. (2009) *J. Cell Biol.* **185,** 1275–1284
11. Xiong, J. P., Stehle, T., Diefenbach, B., Zhang, R., Dunker, R., Scott, D. L., Joachimiak, A., Goodman, S. L., and Arnaout, M. A. (2001) *Science* **294,** 339–345
12. Xiao, T., Takagi, J., Coller, B. S., Wang, J. H., and Springer, T. A. (2004) *Nature* **432,** 59–67
13. Xiong, J. P., Stehle, T., Zhang, R., Joachimiak, A., Frech, M., Goodman, S. L., and Arnaout, M. A. (2002) *Science* **296,** 151–155
14. Jin, M., Andricioaei, I., and Springer, T. A. (2004) *Structure* **12,** 2137–2147
15. Leahy, D. J., Aukhil, I., and Erickson, H. P. (1996) *Cell* **84,** 155–164
16. Humphrey, W., Dalke, A., and Schulten, K. (1996) *J. Mol. Graphics* **14,** 33–38
17. Puklin-Faucher, E., Gao, M., Schulten, K., and Vogel, V. (2006) *J. Cell Biol.* **175,** 349–360
18. Jorgensen, W. L., Chandrasekhar, J., Madura, J. D., Impey, R. W., and Klein, M. L. (1983) *J. Chem. Phys.* **79,** 926–935
19. Phillips, J. C., Braun, R., Wang, W., Gumbart, J., Tajkhorshid, E., Villa, E.,

Chipot, C., Skeel, R. D., Kale, L., and Shulten, K. (2005) *J. Comput. Chem.* **26,** 1781–1802

20. MacKerell, A. D., Bashford, D., Bellott, M., Dunbrack, R. L., Evanseck, J. D., Field, M. J., Fischer, S., Gao, J., Guo, H., Ha, S., Joseph-McCarthy, D., Kuchnir, L., Kuczera, K., Lau, F. T. K., Mattos, C., Michnick, S., Ngo, T., Nguyen, D. T., Prodhom, B., Reiher, W. E., Roux, B., Schlenkrich, M., Smith, J. C., Stote, R., Straub, J., Watanabe, M., Wiorkiewicz-Kuczera, J., Yin, D., and Karplus, M. (1998) *J. Phys. Chem. B* **102,** 3586–3616
21. Craig, D., Gao, M., Schulten, K., and Vogel, V. (2004) *Structure* **12,** 2049–2058
22. Isralewitz, B., Baudry, J., Gullingsrud, J., Kosztin, D., and Schulten, K. (2001) *J. Mol. Graph. Model.* **19,** 13–25
23. Wriggers, W., and Schulten, K. (1997) *Proteins* **29,** 1–14
24. Takagi, J., Petre, B. M., Walz, T., and Springer, T. A. (2002) *Cell* **110,** 599–611
25. Katz, A. K., Glusker, J. P., Beebe, S. A., and Bock, C. W. (1996) *J. Am. Chem. Soc.* **118,** 5752–5763
26. Mould, A. P., Askari, J. A., Barton, S., Kline, A. D., McEwan, P. A., Craig, S. E., and Humphries, M. J. (2002) *J. Biol. Chem.* **277,** 19800–19805
27. Valdramidou, D., Humphries, M. J., and Mould, A. P. (2008) *J. Biol. Chem.* **283,** 32704–32714
28. Lu, H., and Schulten, K. (2000) *Biophys. J.* **79,** 51–65
29. Luo, B. H., Karanicolas, J., Harmacek, L. D., Baker, D., and Springer, T. A. (2009) *J. Biol. Chem.* **284,** 3917–3924
30. Barton, S. J., Travis, M. A., Askari, J. A., Buckley, P. A., Craig, S. E., Humphries, M. J., and Mould, A. P. (2004) *Biochem. J.* **380,** 401–407
31. Shimaoka, M., Xiao, T., Liu, J. H., Yang, Y., Dong, Y., Jun, C. D., McCormack, A., Zhang, R., Joachimiak, A., Takagi, J., Wang, J. H., and Springer, T. A. (2003) *Cell* **112,** 99–111
32. Chen, J., Salas, A., and Springer, T. A. (2003) *Nat. Struct. Biol.* **10,** 995–1001
33. Mould, A. P., Barton, S. J., Askari, J. A., Craig, S. E., and Humphries, M. J. (2003) *J. Biol. Chem.* **278,** 51622–51629
34. Thomas, W. E., Trintchina, E., Forero, M., Vogel, V., and Sokurenko, E. V. (2002) *Cell* **109,** 913–923
35. Guo, B., and Guilford, W. H. (2006) *Proc. Natl. Acad. Sci. U.S.A.* **103,** 9844–9849
36. Marshall, B. T., Long, M., Piper, J. W., Yago, T., McEver, R. P., and Zhu, C. (2003) *Nature* **423,** 190–193
37. Sarangapani, K. K., Yago, T., Klopocki, A. G., Lawrence, M. B., Fieger, C. B., Rosen, S. D., McEver, R. P., and Zhu, C. (2004) *J. Biol. Chem.* **279,** 2291–2298
38. Zhu, C., Lou, J., and McEver, R. P. (2005) *Biorheology* **42,** 443–462
39. Thomas, W. E., Vogel, V., and Sokurenko, E. (2008) *Annu. Rev. Biophys.* **37,** 399–416
40. Tchesnokova, V., Aprikian, P., Yakovenko, O., Larock, C., Kidd, B., Vogel, V., Thomas, W., and Sokurenko, E. (2008) *J. Biol. Chem.* **283,** 7823–7833
41. Yakovenko, O., Sharma, S., Forero, M., Tchesnokova, V., Aprikian, P., Kidd, B., Mach, A., Vogel, V., Sokurenko, E., and Thomas, W. E. (2008) *J. Biol. Chem.* **283,** 11596–11605
42. Marinelli, L., Lavecchia, A., Gottschalk, K. E., Novellino, E., and Kessler, H. (2003) *J. Med. Chem.* **46,** 4393–4404
43. Luque, I., and Freire, E. (2000) *Proteins* **4,** (suppl.) 63–71
44. Zhu, J., Luo, B. H., Xiao, T., Zhang, C., Nishida, N., and Springer, T. A. (2008) *Mol. Cell* **32,** 849–861